Comparing Non-Redundant Masking and Filled-Aperture Kernel Phase for Exoplanet Detection and Characterization

Steph Sallum[a,b] and Andy Skemer[a]

[a]UC Santa Cruz, Department of Astronomy and Astrophysics, 1156 High St. Santa Cruz, CA, USA 95062

[b]NSF Astronomy and Astrophysics Postdoctoral Fellow

ABSTRACT

The limitations of adaptive optics and coronagraph performance make exoplanet detection close to λ/D extremely difficult with conventional imaging methods. The technique of non-redundant masking (NRM), which turns a filled aperture into an interferometric array, has pushed the planet detection parameter space to within λ/D. For high Strehl, the related filled-aperture kernel phase technique can achieve resolution comparable to NRM, without a dramatic decrease in throughput. We present non-redundant masking and kernel phase contrast curves generated for ground- and space-based instruments. We use both real and simulated observations to assess the performance of each technique, and discuss their capabilities for different exoplanet science goals such as broadband detection and spectral characterization.

Keywords: observing techniques, data processing, interferometry, exoplanets, high-contrast imaging

1. INTRODUCTION

Direct imaging has recently emerged as a viable planet detection and characterization method. Near- to mid-infrared observations are particularly useful for discovering giant planets, since they have relatively low contrast at these wavelengths.[1] Several molecules that are expected to be in giant planet atmospheres have opacity in this wavelength range,[2] making infrared spectroscopy useful for constraining atmospheric composition. Furthermore, imaging young planets at these wavelengths can constrain evolutionary scenarios such as hot- versus cold-start models, and planetary atmosphere versus circumplanetary accretion disk scenarios.[2–4]

Typical direct imaging planet searches are limited to angular separations of a few λ/D. Point-spread function (PSF) deconvolution algorithms are less effective within these separations due to the small number of resolution elements available.[5] Phase leakage in even the most high-performance coronagraphic observations prevents high contrast detections within $\sim 1-2$ λ/D.[6] These limitations make semi-major axes less than ~ 10 AU accessible for only the most nearby stars.[7] Expanding this detection parameter space to smaller semi-major axes and/or to more distant stars (including nearby star forming regions[8]) requires novel imaging techniques such as interferometry.

1.1 Non-Redundant Masking

Non-redundant masking[9] is well suited for detecting young, giant planets around more distant stars than typical direct imaging surveys. NRM uses a pupil-plane mask to turn a conventional telescope into an interferometric array. The images are the interference fringes formed by the mask, which we Fourier transform to calculate complex visibilities. Since the mask is non-redundant, no two baselines have the same orientation or separation; information from each baseline is encoded in a unique location in Fourier space.

Non-redundancy means that the instrumental component of each Fourier phase can be written as a linear combination of pupil phases. Calculating closure phases,[10] sums of phases around baselines forming a triangle, eliminates these instrumental phases to first order, leaving behind sums of phases intrinsic to the target. Closure phases are particularly powerful for close-in companion detection because they are sensitive to asymmetries. Since

Further author information: (Send correspondence to S.S.)
S.S.: E-mail: ssallum@ucsc.edu

closure phases are correlated, we project them into linearly-independent combinations called kernel phases.[11–13] We also calculate squared visibilities, the powers on each mask baseline.

Despite the low throughput ($\sim 10\%$), NRM's superior PSF characterization probes angular separations at and even within the diffraction limit. It has led to detections of both stellar[14] and substellar companions,[15,16] as well as circumstellar disks[13,17,18] at these small angular separations. This angular resolution means that spatial scales of ~ 10 AU can be resolved for stars ~ 150 pc away. NRM led to the discovery of a promising system for planet formation studies, the protoplanetary candidates in LkCa 15.[14] Dual-aperture LBTI masking observations recently resolved a solar-system sized disk around the star MWC 349A,[18] at a distance of $\gtrsim 1.2$ kpc from Earth. With a maximum baseline of 23 meters, this is a preview of NRM's potential on 30-meter class telescopes. Non-redundant masking on current telescopes and on future facilities will expand the exoplanet detection parameter space.

1.2 Filled-Aperture Kernel Phase

Extreme adaptive optics systems have made filled-aperture kernel phase[11] an interesting alternative to non-redundant masking. Kernel phase involves treating a conventional telescope as if it were a redundant array. Redundancy prevents Fourier phases from being written as a linear combination of pupil-plane phases. However, in the high Strehl regime (where instrumental pupil plane phases are small), one can justify Taylor expanding the instrumental wavefront. This means that the redundant Fourier phases can be approximated as a linear operator on the pupil plane phases. Finding the nullspace of this linear operator yields kernel phases, linearly independent combinations of Fourier phases that are robust to instrumental phase errors to first order. Like closure (and kernel phase) in non-redundant masking, filled-aperture kernel phases are sensitive to asymmetries and are thus powerful for close-in companion detection.

Kernel phase has been demonstrated on archival *Hubble Space Telescope* observations of ultracool dwarfs.[19] In addition to confirming several known companions to these L dwarfs, it led to the detection of five new binary systems at angular separations of $\sim 40-80$ mas at $\sim 1.1-1.7$ μm. It has also been applied to ground-based data from Keck[20] and Palomar,[21] where it led to the detection of stellar and substellar companions at ($\sim 1-2$ λ/D). The Keck observations were taken at M_s band, where the high sky background reduces the SNR of masking observations. These kernel phase datasets provided comparable resolution to that expected for NRM, with a lower integration time.

1.3 Outline of this Paper

Here we compare non-redundant masking and filled-aperture kernel phase in a controlled way, with a specific focus on exoplanet science. We generate simulated datasets for three imagers: NIRC2 on Keck, and NIRCam and NIRISS on *James Webb Space Telescope (JWST)*. We also generate observations for two integral field spectrographs (IFSs): OSIRIS on Keck, and NIRSpec on *JWST*. Integral field spectroscopy is a particularly interesting kernel phase application, since dispersing the light and applying a pupil plane mask would require long integration times for high signal to noise. We use these contrast curves to place detection limits on planetary atmosphere and circumplanetary accretion disk models. We discuss the potential of each technique as a method for exoplanet detection and characterization.

2. EXOPLANET DETECTION: BROADBAND IMAGING

Here we simulate non-redundant masking and filled-aperture kernel phase observations for Keck NIRC2, and *JWST* NIRCam and NIRISS. For both techniques, the observational strategy involves alternating between integrating on the science target and a PSF calibrator. Since Fourier phase noise includes both a rapidly-changing, high-frequency component and a quasi-static ("speckle") component, better calibration is achieved with large amounts of sky rotation. This is because speckle noise will remain fixed on the detector while true astrophysical signals will rotate with the sky. Thus for all datasets in this section and in Section 3 we simulate data on both target and calibrator stars and with varying amounts of total parallactic angle coverage. When possible, we anchor the simulations by comparing them to real datasets.

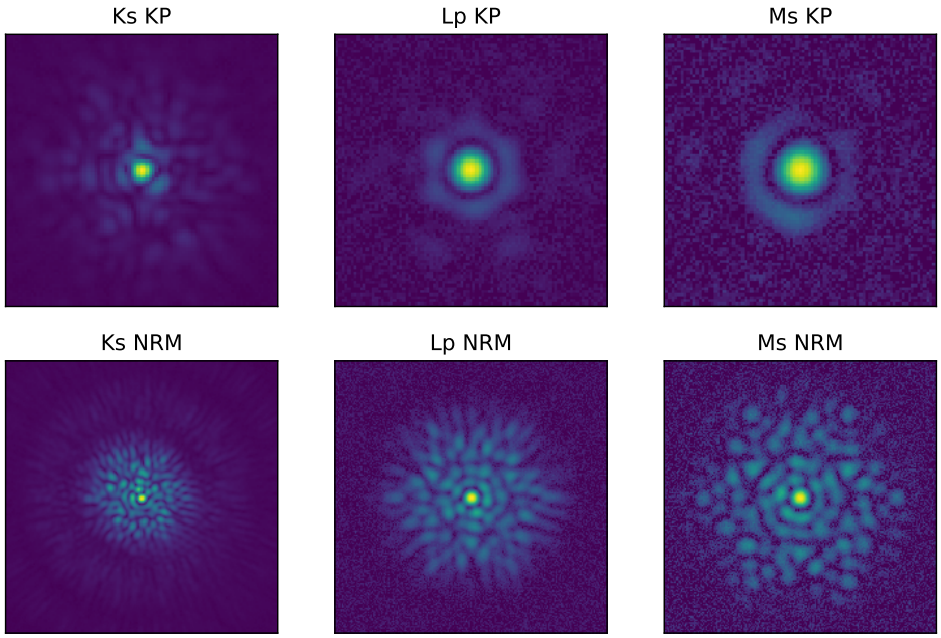

Figure 1 Simulated individual K_s (left), L' (center), and M_s (right) images for the observing parameters listed in Table 1. The top row shows filled-aperture data, and the bottom row non-redundant masking data. The images are displayed on a square root scale to highlight structure in the wings of the point spread function.

2.1 Keck NIRC2

We only have deep (many target pointings over a wide range of parallactic angles) NRM observations at a single NIRC2 observing band (L'). We also only have a single NIRC2 filled-aperture kernel phase dataset without a calibrator observation. We thus generate contrast curves from simulated data to compare non-redundant masking and filled-aperture kernel phase for multiple wavelengths and observing scenarios. We simulate kernel phases for filled-aperture and masked Keck NIRC2 observations at Ks = 2.15 μm, L' = 3.78 μm, and Ms = 4.67 μm.

Keck AO is known to be affected by low-order residual wavefront errors that have been modeled as segment piston errors in the past.[22] To simulate point spread functions, we create optical path difference (OPD) maps that are a combination of low- and high-order residual wavefront errors. We generate low-order errors over the entire Keck pupil and on each individual mirror segment. For the entire pupil, we make combinations of the first 20 Zernike modes (excluding tip and tilt), drawing each coefficient from a uniform distribution. We assume that the width of the Zernike coefficient distribution decreases with the square root of its order, to simulate decreasing residual wavefront error with increasing spatial frequency. We next add tip, tilt, and piston errors to each mirror segment, subtracting off the mean segment tip and tilt to eliminate any shift of the resulting image.

To simulate high-order residual wavefront errors, we begin by generating atmospheric phase screens with von Karman statistics and wind speeds and outer scales consistent with those measured at Mauna Kea.[23] We apply a low pass filter, only allowing frequencies lower than 1 / 2d where d is the Keck actuator spacing, to mimic atmospheric fitting. We then subtract the low pass filtered phase screen from the original phase screen. The typical rms for these simulated residual AO errors is $\sim$ 100 nm, consistent with the fitting errors estimated for Keck AO.[24] We note that imperfect atmospheric fitting is not the only source of high frequency wavefront error; we neglect other sources such as bandwidth error and aliasing. We also do not average many residual phase

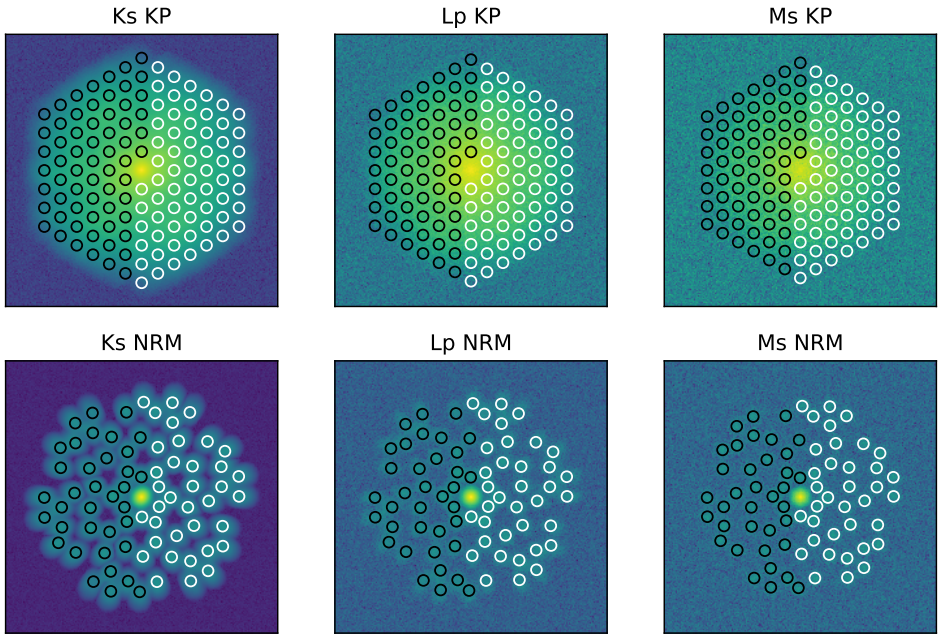

Figure 2 Simulated K_s (left), L' (center), and M_s (right) power spectra for a single frame using the observing parameters listed in Table 1. The top row shows filled-aperture kernel phase data, and the bottom row non-redundant masking data. Random noise from the large sky background is apparent in the L' and M_s power spectra; building signal to noise in the long baselines requires combining more frames.

screens for each science exposure, which would be appropriate for integrations that are long compared to the AO frame rate. These simulated OPDs are thus not an exact representation of the Keck AO system, but they are consistent with our observations (see below) and are similar to OPD models that have been used previously.[23]

In addition to phase errors caused by OPD variations, we also simulate random phase errors by adding Poisson noise from the sky and the target star, dark current, and read noise to the images. We then tune the rms of the low- and high-order residual wavefront error components so that it reproduces the scatter in real, uncalibrated L' NRM and filled-aperture datasets ($\sim 1.0 - 1.5°$), and so that it is consistent with previous estimates of the low- and high-order wavefront error (WFE) rms.[22] This results in rms $\simeq$ 260 nm for the low-order errors, and rms $\simeq$ 100 for the high order errors, for a total residual wavefront error of $\sim$ 280 nm. We check that these optical path difference maps lead to qualitatively similar PSFs as those observed with NIRC2, as well as Strehl ratios consistent with those measured for NIRC2 Ks and L' band images ($\sim$ 60% at Ks and $\gtrsim$ 85% at L'). Figure 1 and 2 show example images and power spectra, respectively for each bandpass and observing technique.

We simulate observing strategies typical of NRM observations: alternating observations between a science target and a calibrator. The number of coadds, number of frames per pointing, and integration times for each filter and mode are listed in Table 1. We simulate datasets with two different amounts of sky rotation evolution: (1) a snapshot with no parallactic angle change, and (2) seven target-calibrator pointings with 65° total parallactic angle change. The second case is comparable to the amount of integration and parallactic angle change that is achievable in a quarter night of Keck Ks and L' NRM observing with overheads.

Keck's low-order errors are quasi-static[25] and contribute to calibration errors in the final kernel phases. We thus generate calibrator observations after evolving the OPD Zernike coefficients by a fraction drawn from a

Table 1. Simulated NIRC2 Observing Parameters

Technique	Filter	t_{coadd} (s)	n_{coadds}	n_{frames}	t_{total} (s)[a]
KP	K_s	0.1	10	20	20
NRM	K_s	1	10	20	200
KP	L'	0.2	10	20	40
NRM	L'	2	10	20	400
KP	M_s	4	10	10	400
NRM	M_s	50	10	5	2500

[a]Total integration time for a single target observation consisting of n_{frames} frames ($t_{coadd} \times n_{coadds} \times n_{frames}$).

zero-mean uniform distribution with width f. We use the original and evolved optical path difference maps to generate point spread functions for each target and calibrator observation, respectively. To calibrate, we subtract the simulated calibrator kernel phases from the target kernel phases. We tune the evolution fraction, f, so that the calibration decreases the kernel phase scatter the same amount as it does in typical NIRC2 NRM observations ($f = 0.8$). Figure 3 shows an example of OPD evolution for both techniques; the residual OPD map has ~ 50 nm rms low order errors and ~ 90 nm rms high order errors.

Figure A.1 shows histograms of the raw (uncalibrated) and calibrated kernel phases for each technique and bandpass. At L' and M_s, where the Strehl is high, the scatter in the raw kernel phases is comparable between filled-aperture and masked datasets. At K_s, the raw kernel phase scatter is much higher for filled-aperture datasets than for NRM observations. Furthermore, in all cases the calibration reduces the NRM kernel phase scatter more than the filled-aperture kernel phase scatter. This shows that instantaneous OPD as well as changing OPDs degrade filled-aperture kernel phases more significantly than NRM kernel phases.

To generate contrast curves, we fit a grid of single companion models to calibrated observations of single point sources. We calculate a $\Delta\chi^2$ between each companion model and the null model, to find the probability that each companion model would be spuriously detected. For each separation, we take our 5σ contrast to be the companion contrast detected with a $\Delta\chi^2$ of 31.82 relative to the null model (since the companion models have three degrees of freedom). To make the final contrast curve for each of these, we average the $\Delta\chi^2$ maps for more than ten different simulated datasets. We check that these contrast curves based on Type 1 errors match those based on Type 2 errors (companion injection and recovery). We also check that the simulations reproduce the contrast curve calculated from L' NRM observations (see Figure 4).

Figure 5 compares the kernel phase and non-redundant masking contrast curves for all three NIRC2 bandpasses. At Ks band, where the Strehl is relatively low ($\sim 0.5 - 0.6$), the achieved kernel phase contrast is lower than the NRM contrast at all angular separations. For L' and Ms bands, kernel phase provides comparable or higher contrast at angular separations outside of λ/D. However, at lower separations NRM achieves slightly higher contrast (by ~ 0.5 mag).

We convert our 5σ contrast curves to planet mass limits using DUSTY models,[26] as well as circumplanetary accretion disk models.[3,4] For the DUSTY models, we assume an age of ~ 5 Myr, since the moderate contrast offered by both techniques makes them most useful for detecting young planets around distant targets. Figures 6 and 7 show the planet and accretion disk limits, respectively, for a range of separations and stellar absolute magnitudes. Depending on the stellar magnitude, both NRM and kernel phase can constrain planet masses of a few to ten Jupiter masses, or planet masses times accretion rates of $\sim 10^{-6}$ M_J^2 yr^{-1}. We note that these mass limits would be lower for younger planets.

We note that both the limiting magnitude of the AO system and a high sky background would make it difficult to access the upper regions of these plots from the ground, especially for distant targets. The white

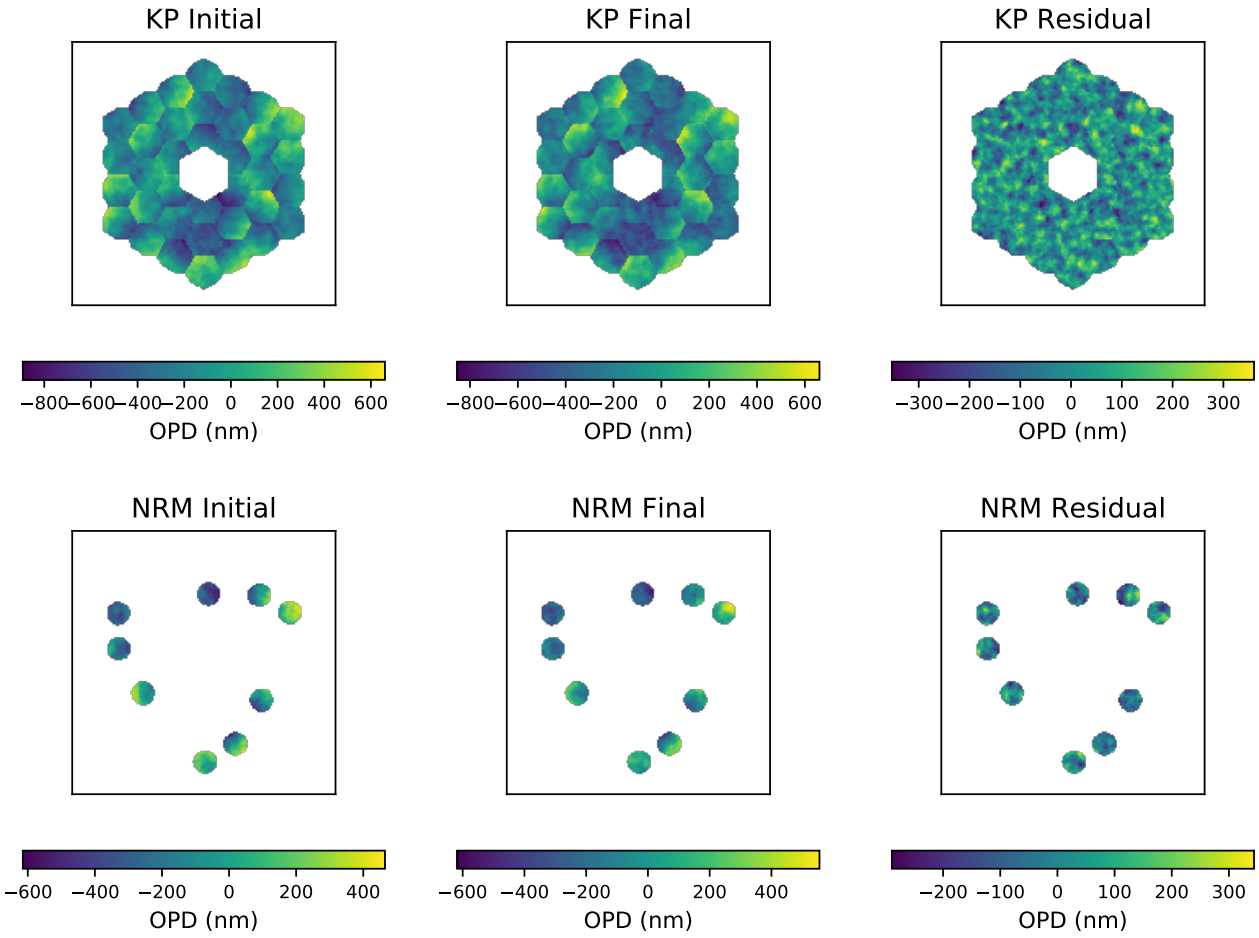

Figure 3 Example OPD evolution for NIRC2 filled-aperture kernel phase (top) and non-redundant masking (bottom). The left shows an initial OPD made up of both low- and high-order wavefront errors, and the center panel shows the result of evolving the low-order WFE and combining it with a different random high-order OPD. The right side shows the difference between the two; it has an rms OPD of ~ 104 nm (~ 50 nm low-order and ~ 90 nm high-order).

dotted line in Figure 6 and 7 indicates the absolute magnitude of a 5 Myr old K5 star[27] at a typical distance to nearby star forming regions (~ 140 pc[8]). Its R band magnitude of ~ 11, compared to the Keck NGS limiting magnitude of $\sim 14-16$, means that observations of similarly red and distant objects would be feasible only in the bottom half of the panels in Figures 6 and 7.

2.2 JWST: NIRCam Kernel Phase Versus NIRISS Aperture Masking Interferometry

We use the Pandeia engine[28] and WebbPSF software[29] to simulate NIRCam kernel phase and NIRISS aperture masking observations to compare the two techniques. Since exoplanets are relatively bright in the near- to mid-infrared, we simulate data for filters centered on wavelengths $\gtrsim 4$ μm (F430M and F480M). Rather than choose a specific target spectrum and distance for each simulated observation, we assume a flat spectrum over each bandpass ($f_\nu = 0.1$ Jy, $m_{ab} \sim 11.4$) and tune the number of groups to maximize the signal to noise (SNR) in a single integration without saturating. We ultimately analyze a cube of integrations for each observation (see below). Table 2 lists the specific parameters we use for each instrument. We note that these simulations are

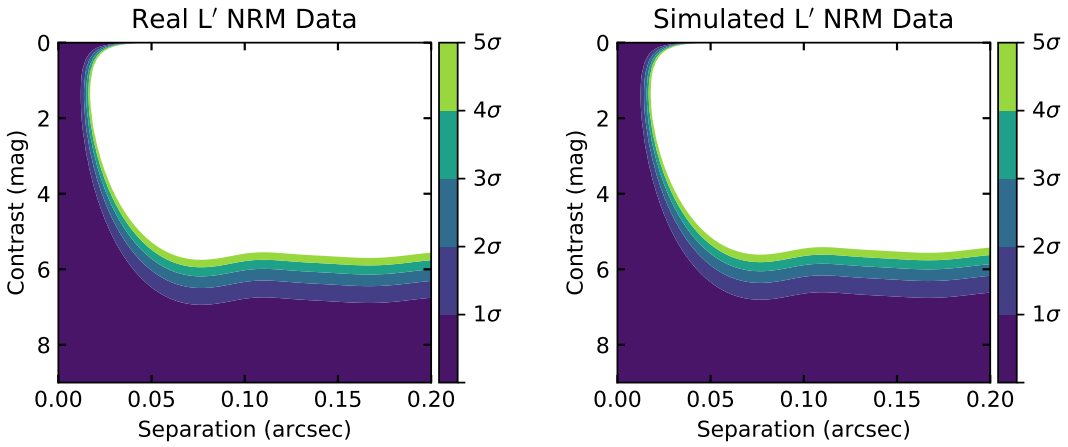

Figure 4 Contrast curves for a single target observation made from real L′ NIRC2 NRM observations (left), and simulated observations (right). The contrast curves are nearly identical, with 5σ contrast of > 5.5 magnitudes.

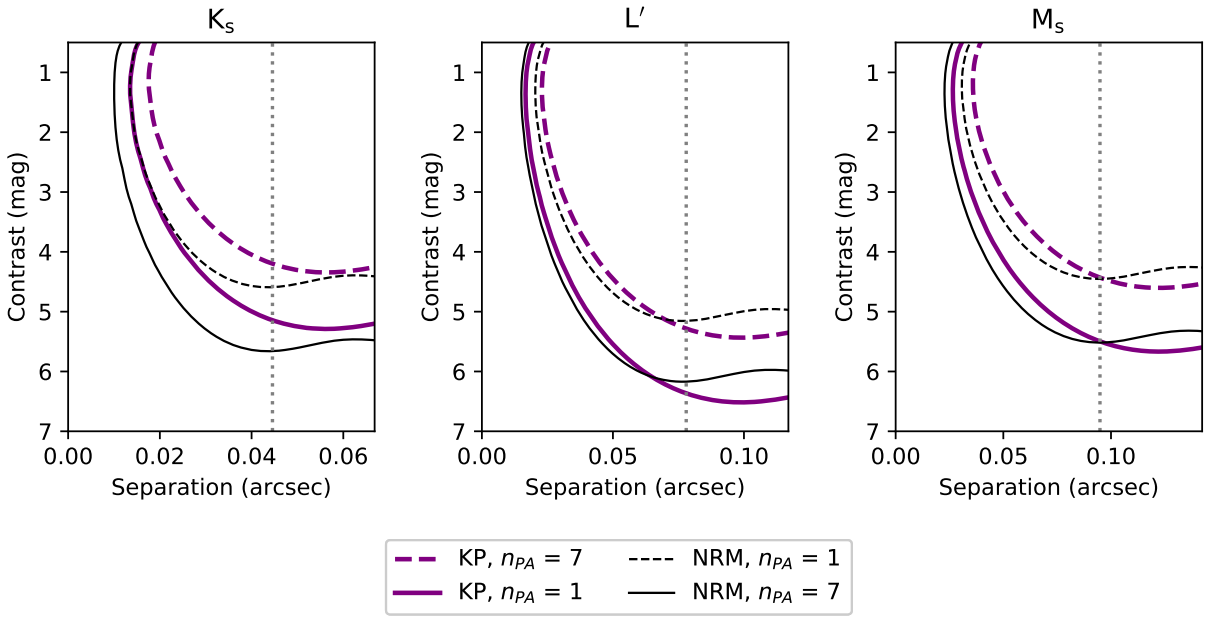

Figure 5 Kernel phase (thick purple lines) and NRM (thin black lines) contrast curves for snapshot datasets (dashed lines) and datasets with 7 different parallactic angles with 65° of sky rotation. In each panel, the vertical dotted line marks λ/D in the observing bandpass.

still relevant for targets with different $\sim 4-5$ μm fluxes, which may require different integration times (t_{int}) to achieve comparable SNR.

For each pointing, we generate science target and calibrator frames using different optical path difference maps to simulate PSF evolution. We begin by randomly choosing one of ten optical path difference maps included in WebbPSF. We then fit a hexike basis to each mirror segment, including up to 100 coefficients. We evolve each of the hexike coefficients by a fraction drawn from a uniform distribution with σ tuned to result in two different rms residual WFEs: $\sim$ 10 nm in the optimistic case, and $\sim$ 40 nm in the pessimistic case. For both NIRCam

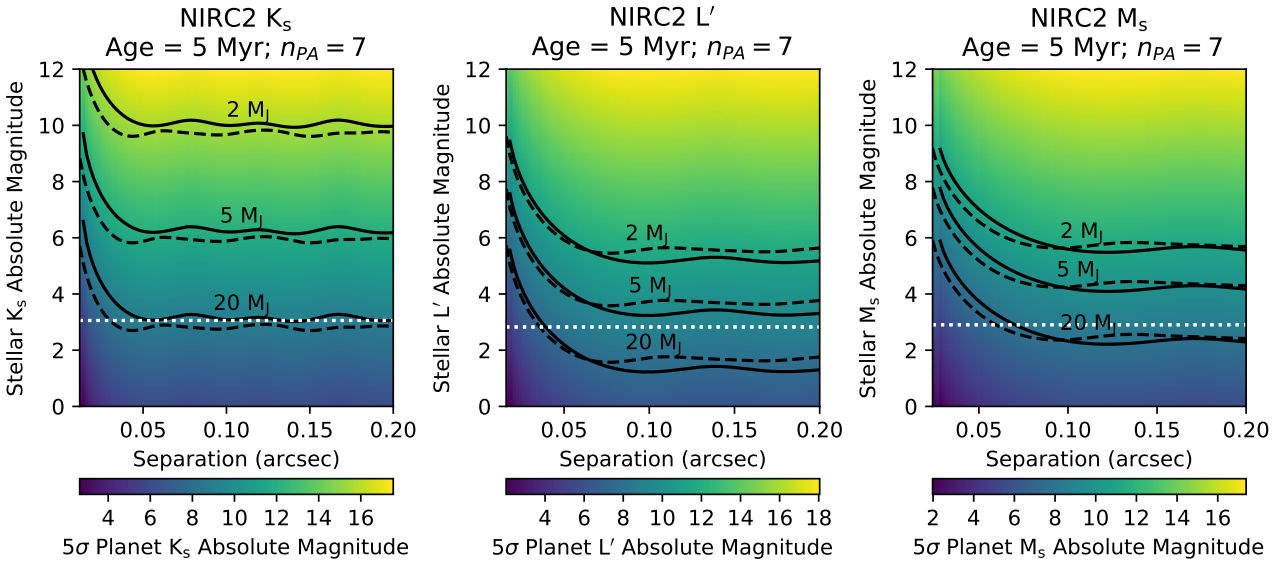

Figure 6 Five σ planet mass limits using 5 Myr DUSTY models for the datasets with 7 different parallactic angles covering 65°. The solid and dashed curves show limits for kernel phase and aperture masking, respectively. The white dotted line shows the absolute magnitude of a 5 Myr old K5 star at a typical distance to nearby star forming regions ($\sim$ 140 pc).

Table 2. Simulated JWST Observing Parameters

Instrument	Filter	f_{source} (Jy)	n_g	t_{int} (s)[a]	SNR	t_{total} (s)[b]
NIRCam	F430M	0.1	9	0.5	321.70	200
NIRCam	F480M	0.1	12	0.65	338.88	260
NIRISS	F430M	0.1	250	18.94	324.42	7576
NIRISS	F480M	0.1	250	18.94	339.94	7576

[a]Integration time for a single frame consisting of n_g groups.

[b]Total integration time for all frames in each observation datacube ($t_{int} \times$ 400).

and NIRISS, these correspond to $\sigma = 0.2$ and $\sigma = 0.65$, respectively. Figure 8 shows an example initial, final, and residual OPD map for a single rms $\simeq$ 10 nm simulation for both instruments, and Figure 9 shows example images and power spectra.

For all instrument / filter combinations, we analyze a cube of 400 images for each observation.* We average the raw kernel phases for all integrations for each target and calibrator observation, and then subtract the calibrator kernel phases from the target. For both NIRCam and NIRISS, we assume two target-calibrator pairs observed at roll angles 45° apart. Figure A.2 compares the raw and calibrated NIRCam filled-aperture kernel phases, and NIRISS NRM kernel phases for the 10 nm rms WFE case. While the raw kernel phase scatter is

*We note that cube lengths $\gtrsim$ 100 frames would produce comparable calibrated kernel phase scatter. The t_{total} values in Table 2 are for 400 frames.

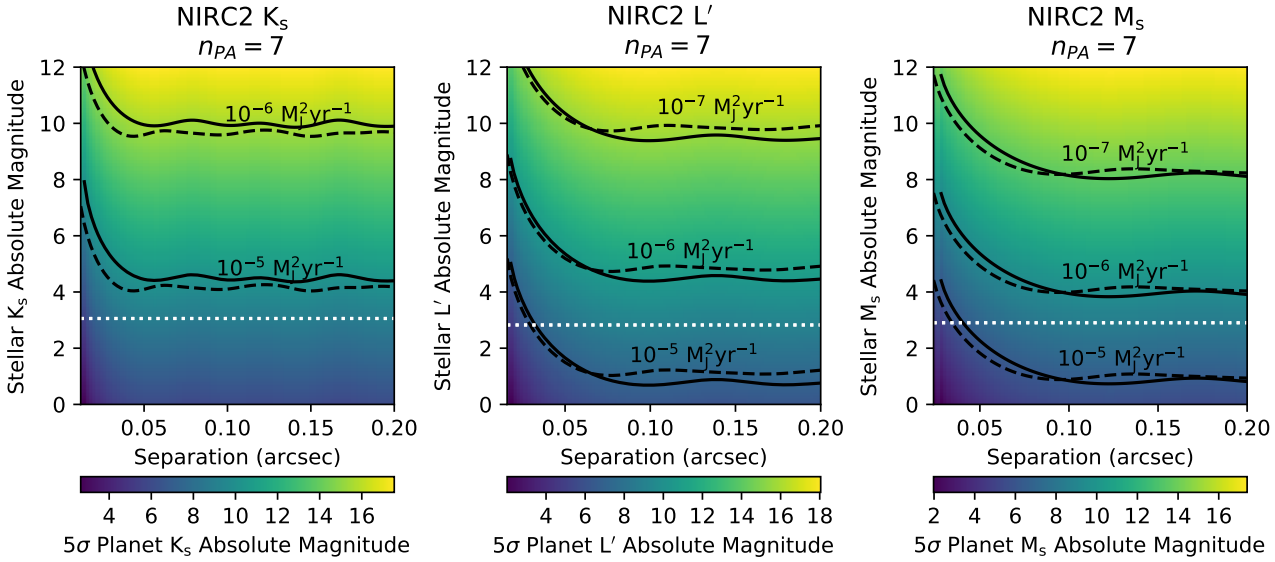

Figure 7 Five σ circumplanetary accretion disk (planet mass times accretion rate) limits for the datasets with 7 different parallactic angles covering 65°. The solid and dashed curves show limits for kernel phase and aperture masking, respectively. The white dotted line shows the absolute magnitude of a 5 Myr old K5 star at a typical distance to nearby star forming regions ($\sim$ 140 pc).

slightly lower for NIRCam in both filters, the calibrated scatter is comparable for NIRCam and NIRISS. This suggests that OPD evolution impacts filled-aperture kernel phase more negatively than masked kernel phase.

We calculate contrast curves for the calibrated data in the same way as we do for the NIRC2 datasets (see Section 2.1). Figure 10 compares the 5 σ contrast curves for NIRCam and NIRISS within the first $\sim$ 200 mas. Like NIRC2, NRM on NIRISS achieves higher contrast than NIRCam kernel phase by $\sim$ 0.5 mag within λ/D. At larger separations, filled aperture kernel phase and NRM achieve comparable contrast.

Figures 11 and 12 show the 5σ planet and circumplanetary accretion disk limits for a range of stellar absolute magnitudes and separations. The greater stability of JWST leads to higher contrast than that achieved with NIRC2, making lower mass planets and lower accretion rates more accessible for brighter stars. Furthermore, since JWST is not limited by sky background or adaptive optics performance, it is much more feasible to reach the upper regions of the individual panels. The white dotted line in Figures 11 and 12 shows the absolute magnitude for a 5 Myr K5 star at 140 pc. Depending on the spectral type, distance, and planet age, $\sim$ Jupiter mass planets and planet masses times accretion rates less than 10^{-6} M_J^2 yr^{-1} are detectable at the 5σ level. We note that these observations are only for two roll angle positions; datasets with more roll angles would have improved planet mass / accretion rate limits.

The pipeline we used to process the simulated data works with the Fourier transformed images and does not model the images themselves. Fourier-based pipelines deal more poorly with large pixels than image modeling pipelines.[30] However, the pixel sizes for NIRISS and NIRCam are identical at the filters where we make this comparison. Thus any effects due to large pixel size affect both contrast curves; applying an image modeling pipeline would scale them equivalently.

3. EXOPLANET CHARACTERIZATION: INTEGRAL FIELD SPECTROSCOPY

Here we simulate kernel phase observations for two integral field spectrographs: Keck OSIRIS and *JWST* NIRSpec. Since neither of these instruments has a non-redundant masking mode, we simulate only filled-aperture

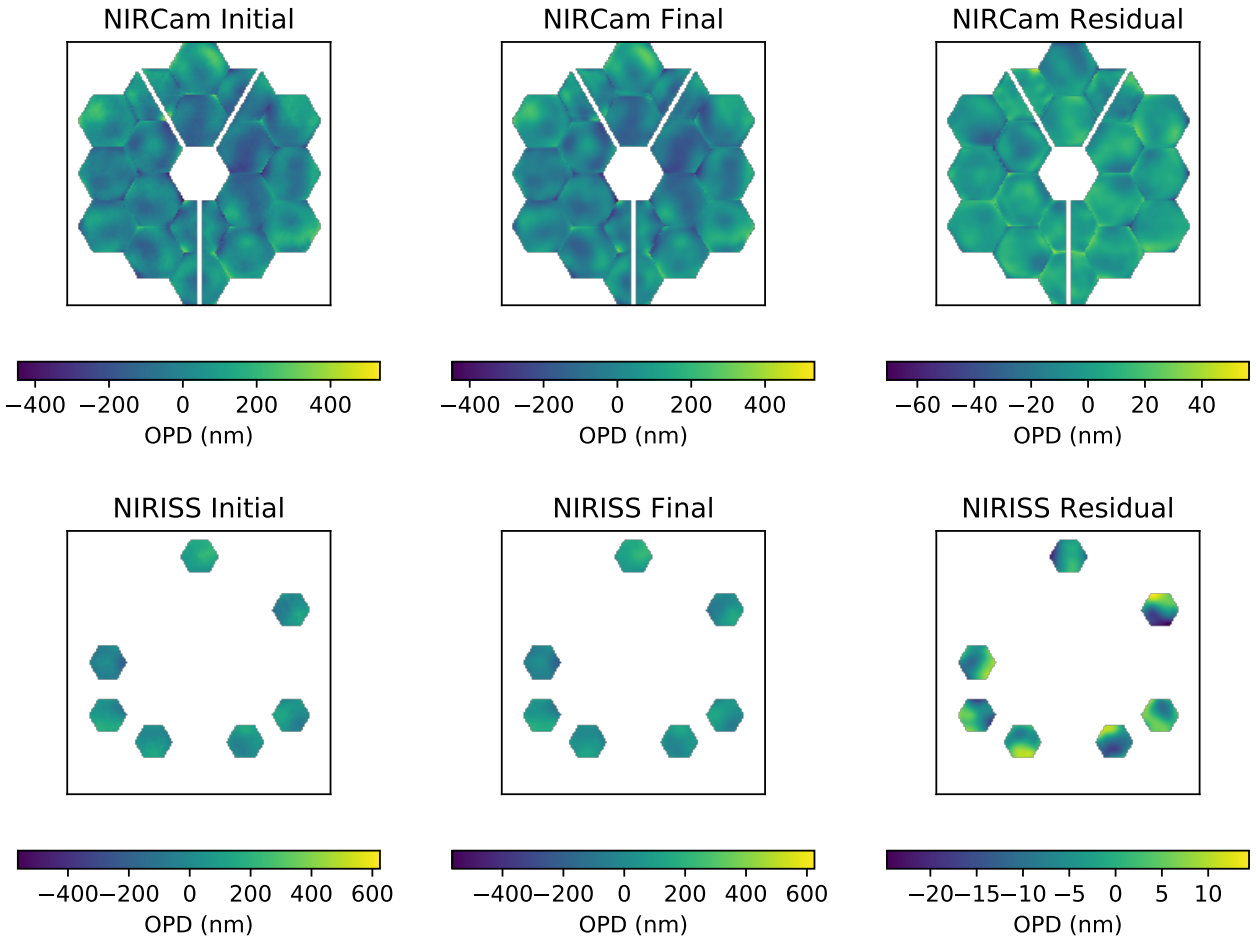

Figure 8 Example JWST optical path difference (OPD) evolution. The left panels show one of ten predicted NIRCam (top) and NIRISS (bottom) optical path difference files from WebbPSF. The center panels shos the resulting OPDs after fitting hexikes to each JWST mirror segment and evolving their coefficients by a small fraction in random directions. The right panels show the difference between the first two OPD maps, and have RMS residual optical path differences of ~ 10 nm.

kernel phase datasets. We assume a similar observing strategy as for the previous instruments: alternating target and calibrator observations while allowing the sky to rotate.

3.1 Keck OSIRIS

OSIRIS is a K band integral field spectrograph on Keck. We simulate OSIRIS kernel phase observations in the Kn3 bandpass, since it covers the accretion-tracing emission line Br-γ, which would be of interest for observing protoplanet candidates. This mode contains 433 wavelength bins between 2.121 and 2.229 microns, for a single bin width of 0.25 nm. We assume a K = 7 target star, using a single 200 second coadd for each frame, and for each target and calibrator pointing we analyze cubes of 20 frames. The total integration time for a single pointing is 4000 seconds. Figure 13 shows an example image and power spectrum.

We generate optical path difference maps in the same way as for NIRC2, evolving the low-order wavefront error between simulated target and calibrator observations. Compared to broadband imaging, IFS observations take longer to build up signal to noise due to the narrow wavelength bins. Thus we do not simulate as deep

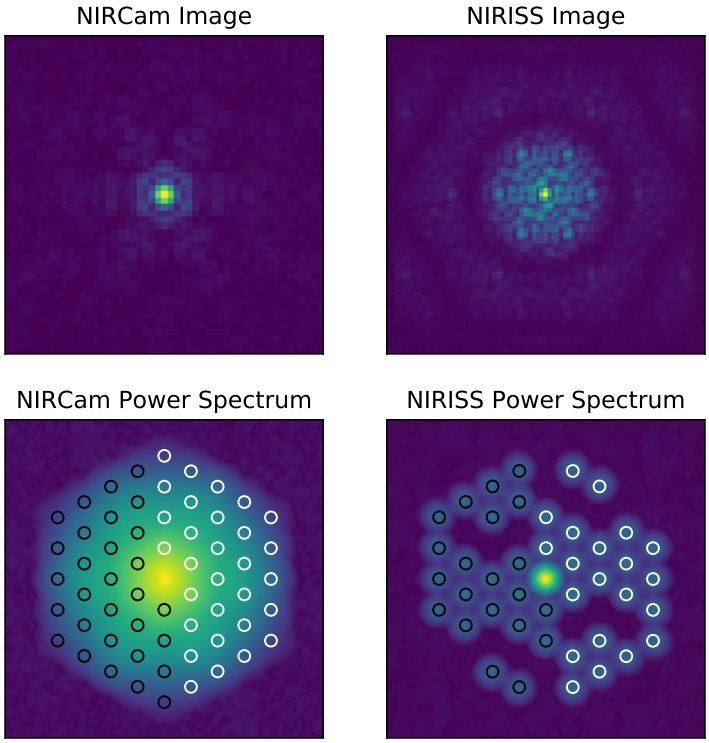

Figure 9 Simulated NIRCam (left) and NIRISS (right) integrations (top) and power spectra (bottom). This dataset uses the F430M filters, the observing parameters listed in Table 2, and residual OPD files comparable to those in Figure 8 The scattered points show the sampling locations for calculating kernel phase; they are shown in two colors since the Fourier transform is symmetric.

datasets as those for NIRC2. We simulate a snapshot, single target-calibrator observation, and a dataset with four target-calibrator pairs spaced evenly over 20° of parallactic angle evolution. As for NIRC2, in addition to phase noise from residual AO errors, we add Poisson noise from the target and sky, dark current, and read noise.

Figure A.4 shows histograms of the raw and calibrated kernel phases. Both the raw and calibrated kernel phases have ~ 1.5 times the scatter of those for NIRC2 at K_s. This could be due to increased random errors, since the throughput of a single wavelength bin for OSIRIS is 1700 times less than the NIRC2 K_s band, but the OSIRIS exposure time is only 200 times greater than that for NIRC2.

We generate contrast curves in the same way as for NIRC2 (see Section 2.1). We use a conservative approach, treating individual slices in the reconstructed data cubes as if they were independent. This assumes no prior knowledge of the target or calibrator spectrum. Figure 14 shows contrast curves generated for both parallactic angle cases for the central Kn3 wavelength bin ($\lambda_c = 2.175$ μm). For the central wavelength bin, OSIRIS can reach contrasts of $\sim 4.5 - 5.5$ magnitudes, depending on the depth of the dataset.

We convert the 5σ contrasts to both 5 Myr planet mass[26] and circumplanetary accretion disk limits,[3,4] as shown in Figures 15 and 16, respectively. The achievable contrasts translate to 5σ mass limits of ~ 20 M_J at 5 Myr, or planet mass times accretion rate limits of $\sim 10^{-5}$ M_J^2 yr^{-1}, for a K5 star at a distance typical of nearby star forming regions. These planet mass / accretion rate limits would become lower with calibration techniques such as spectral differential imaging (SDI),[31] which has been shown to improve contrast by a factor of ~ 10 over calibrations that do not use spectral information.[32]

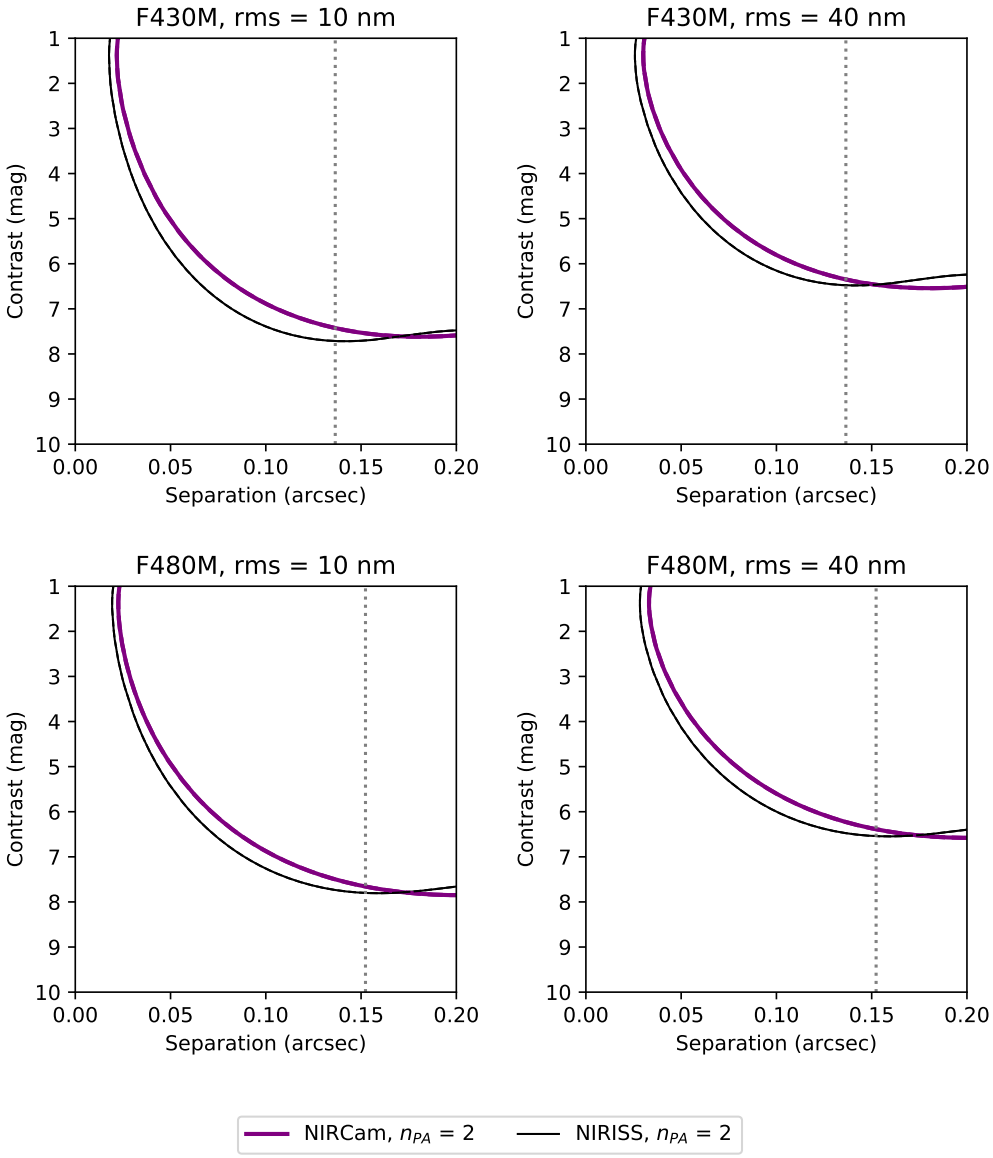

Figure 10 Contrast curves for F430M (top) and F480M (bottom) filters, with the two OPD evolution cases of 10 nm RMS (left) and 40 nm RMS (right). Thick purple lines show NIRCam filled-aperture kernel phases, while thin black lines show NIRISS NRM kernel phases.

3.2 JWST NIRSpec

We use the Pandeia engine and WebbPSF software to generate simulated data for NIRSpec IFU observations. As for NIRCam / NIRISS we simulate observations for a source with a flat spectrum at 0.1 Jy ($m_{ab} \sim 11.4$). We use the G395H grating and the F290LP filter, which yields $\gtrsim 4000$ wavelength bins from 2.87 to 5.27 microns. We follow the same methods for OPD evolution and calibration as for NIRCam / NIRISS, evolving the hexike coefficients by a fraction $f \sim 0.11$ to achieve 10 nm rms residual OPD. We use an integration time of 64.4 seconds per frame (6 groups in NRSRAPID), and analyze 50 frames per pointing.

Since the NIRSpec spaxels are 0.1 arcseconds across they do not Nyquist sample the PSF. We thus generate

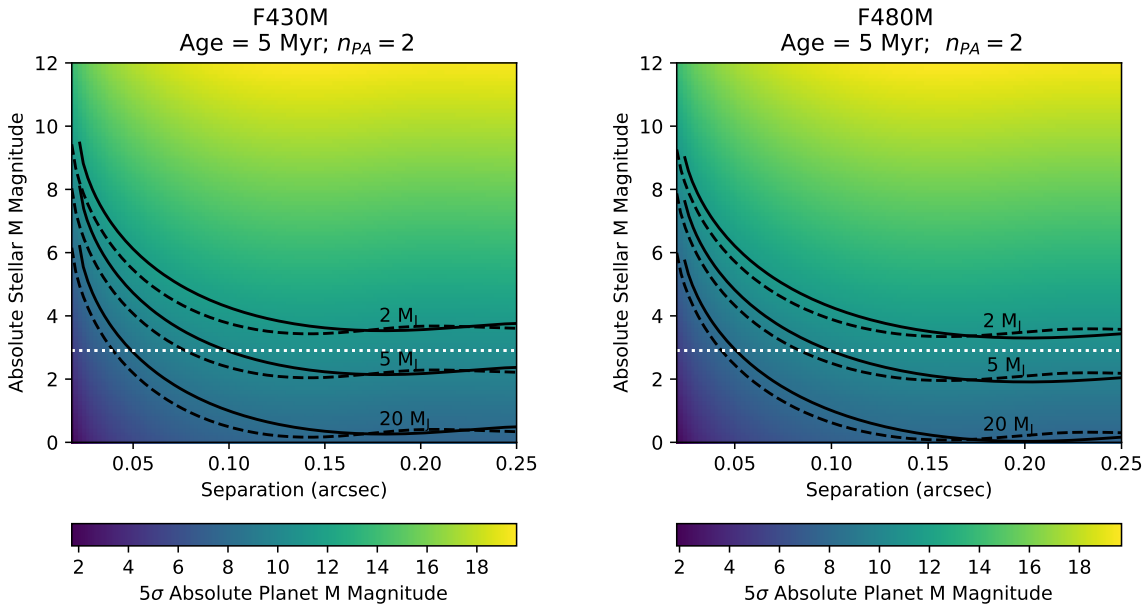

Figure 11 F430M (left) and F480M (right) planet mass limits for 5 Myr DUSTY models for the 10 nm RMS OPD cases. The solid curves show NIRCam kernel phase and the dashed curves show NIRISS non-redundant masking. The white dotted line shows the absolute magnitude of a 5 Myr old K5 star a typical distance to nearby star forming regions ($\sim$ 140 pc).

a 5-pointing small grid dither for each target observation. We create an interpolated Nyquist sampled image ($\sim$ 0.03 arcsecond pixels) from the small grid dither, using Modified Shepard weighting, before taking the Fourier transform to calculate kernel phases. Figure 17 shows examples of these images and an interpolated power spectrum.

Since the NIRSpec observations are time consuming (5 different dither positions to create one Nyquist sampled image), we create contrast curves for a single target - calibrator observing sequence. We calculate contrast curves for an individual wavelength bin (the central bin in the bandpass; $\lambda_c = 4.07$ μm) in the same way as for OSIRIS. Figure 18 shows these; at separations $\gtrsim$ 0.125 arcseconds, contrasts of $\sim$ 5.5 magnitudes can be achieved for a snapshot observation.

Converting these contrast curves to planet mass limits shows that planets of $10 - 20$ Jupiter masses will be detectable for 5 Myr old K5 stars at distances of $\sim$ 140 pc (see Figure 19). Circumplanetary accretion with planet mass times accretion rates of $10^{-6} - 10^{-5}$ M_J^2 yr^{-1} will be measurable for typical stars at that distance. SDI would improve these mass / accretion rate limits, since it could increase the achievable contrast by a factor of ~ 10.[32] Lower mass / accretion rate planets will be detectable around stars with absolute magnitude $\gtrsim 7$ at separations > 100 mas, which will be more easily accessed using *JWST* than ground-based AO observations.

4. DISCUSSION

The contrast curves and derived planet mass / accretion rate limits for NIRC2, NIRCam, and NIRISS show that filled-aperture kernel phase is a viable alternative to non-redundant masking for high Strehl ($\sim 0.8 - 0.9$) observations. This corresponds to wavelengths redder than $\sim$ 3.8 microns for ground-based observations. At these wavelengths, the sky brightness is a lesser problem for kernel phase observations, since the NRM point spread function is spread out over more pixels than the conventional PSF. Space based observations with a

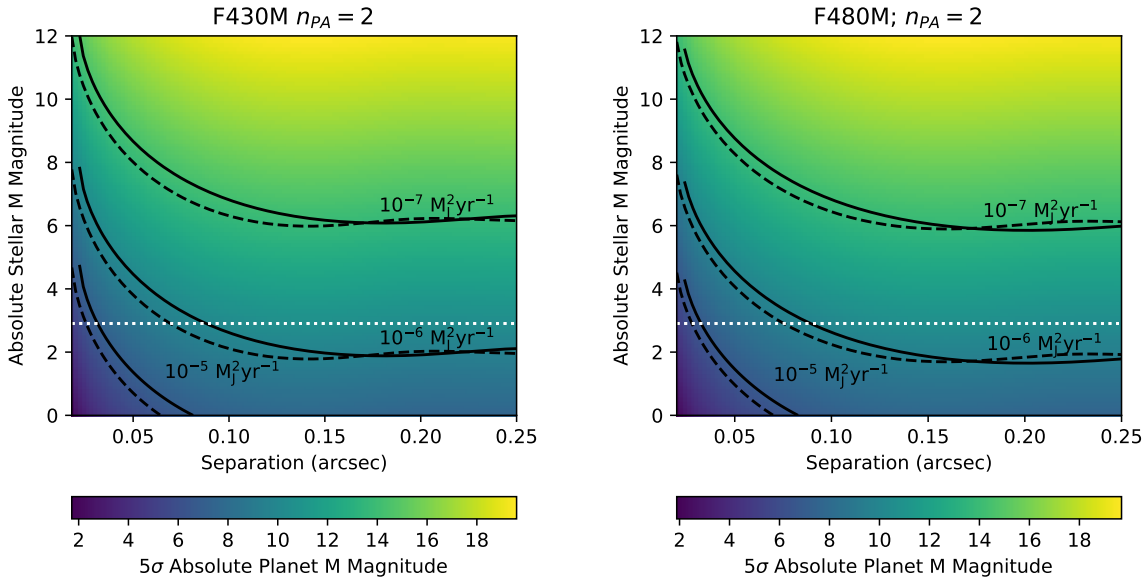

Figure 12 F430M (left) and F480M (right) circumplanetary accretion disk models for the 10 nm RMS OPD cases. The solid curves show NIRCam kernel phase and the dashed curves show NIRISS non-redundant masking. The white dotted line shows the absolute magnitude of a few Myr old K5 star at a typical distance to nearby star forming regions ($\sim$ 140 pc).

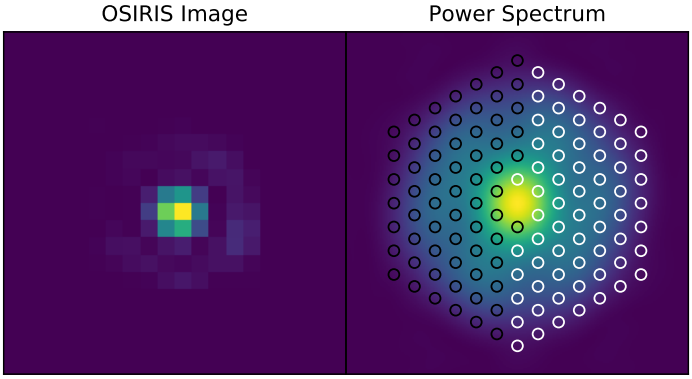

Figure 13 Example simulated OSIRIS image (left) and power spectrum (right).

thermal background would also benefit from kernel phase for the same reason. For both Keck and *JWST*, kernel phase can achieve comparable contrast to NRM at separations outside λ/D. However, at angular separations within λ/D, non-redundant masking will provide slightly higher contrast ($\sim 0.5 - 1$ mag) than filled-aperture kernel phase.

While NRM can provide slightly higher contrast close-in, the required integration times are much longer - a factor of $\sim 10 - 30$ to achieve similar signal to noise as kernel phase. Thus, for very faint stars where building SNR is time consuming, or where a thermal background may wash out the target signal, it may make sense to use filled-aperture kernel phase to save time. This would also be useful in the context of a large survey for young

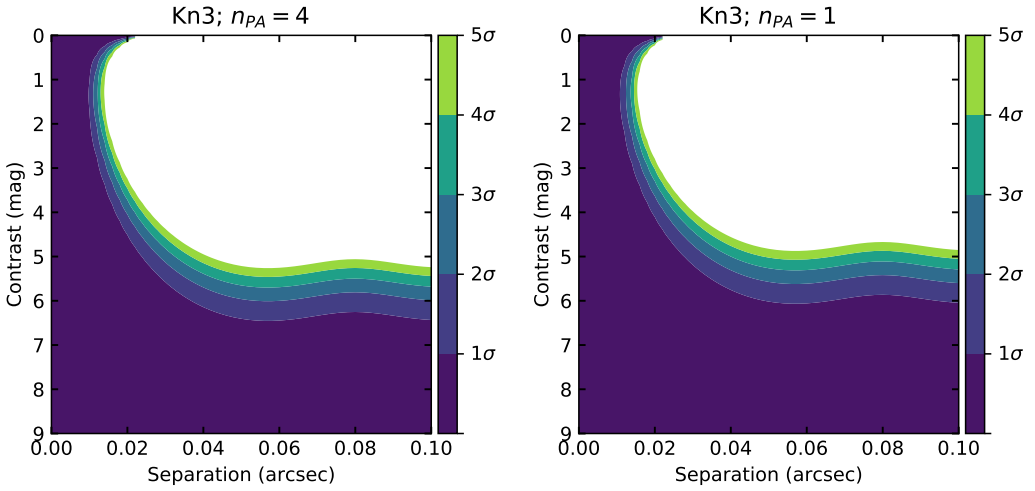

Figure 14 OSIRIS contrast curves for the four parallactic angle simulated data (left) and the single snapshot data (right). These are for a single wavelength bin in the center of the Kn3 bandpass ($\lambda_c = 2.175$ μm).

planets, since the two techniques can place similar constraints on (accreting) planet populations. NRM's better performance suggests that an intermediate case such as a redundant mask may be the ideal observing setup for carrying out faster observations without a loss in contrast.

The OSIRIS and NIRSpec simulations show that kernel phase on an IFS can reach contrasts of $5-6$ magnitudes depending on the dataset depth and Strehl. This is an exciting mode for characterizing young planets at smaller angular separation than that typically achieved with an IFS. For fully-formed planets, this will lead to better atmospheric constraints than possible with narrowband imaging.[1] For accreting planets, it will help to distinguish between different formation scenarios: e.g. hot-start versus circumplanetary disk accretion.[3,4,16] The single-bin contrast curves show that kernel phase on an integral field spectrograph is capable of simultaneous detection and characterization; individual wavelength bins can be treated independently. Furthermore, additional calibration techniques such as spectral differential imaging[31] could help to boost contrast, making lower mass planets and/or lower accretion rates detectable.

The broadband simulations showed an improvement in both achievable contrast and planet mass / accretion rate limits at L′ and Ms, compared to Ks. This suggests that a mid-infrared integral field spectrograph would be particularly useful for planet characterization with these techniques. Arizona Lenslets for Exoplanet Spectroscopy (ALES)[33] on the Large Binocular Telescope is a $3-5$ μm integral field spectrograph with a non-redundant masking mode. ALES' redder wavelength range should lead to higher contrast (and lower planet mass / accretion rate limits) compared to other ground-based integral field spectrographs. ALES has not yet been characterized for non-redundant masking or filled-aperture kernel phase observations; this will be the subject of future work.

Both NRM and filled-aperture kernel phase, applied on *James Webb* have the potential to expand the planet detection parameter space beyond that of ground-based observations. While *JWST* does not have higher resolution than current ground-based facilities, its greater stability means that it can reach much higher contrasts. Furthermore, it will not have the same limitations on target star brightness as an AO-corrected telescope does. These factors combined mean that *JWST* will detect and characterize lower mass / accretion rate planets than we can observe from the ground.

5. CONCLUSIONS

We presented contrast curves for non-redundant masking and filled-aperture kernel phase on several broadband imagers and integral field spectrographs. While most of these observations were simulated, when possible we

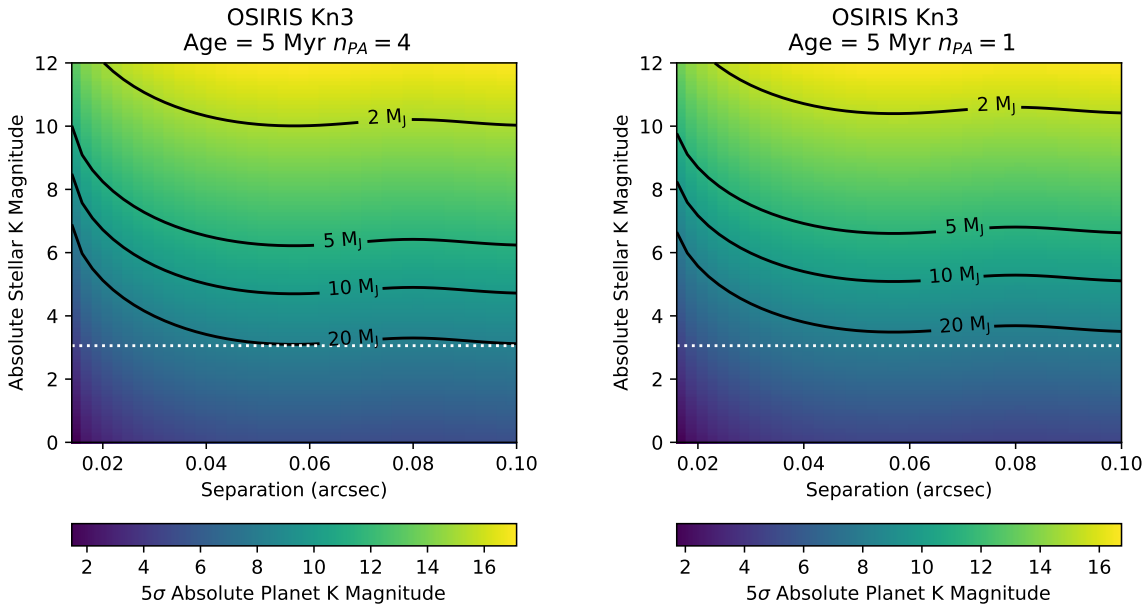

Figure 15 Planet mass limits for 5σ contrast in the central Kn3 wavelength bin as a function of stellar absolute magnitude. The colorscale shows the 5σ planet absolute magnitude, and the contours show DUSTY models for an age of 5 Myr. The left panel shows the four parallactic angle case, and the right shows the single snapshot case. The white dotted line shows the absolute magnitude of a 5 Myr old K5 star at a typical distance to nearby star forming regions ($\sim$ 140 pc).

used real observations to anchor our OPD generation prescription. The simulated contrast curves show that for high Strehl, kernel phase can perform comparably to or better than NRM outside of λ/D. Closer in, masking outperforms filled-aperture kernel phase by $0.5 - 1$ magnitudes. This slightly lower contrast suggests that redundant masks may be a good compromise to reach high contrast with shorter exposure times than NRM.

Both NRM and kernel phase are capable of detecting giant, recently-formed planets, or accretion signatures from forming planets. Filled-aperture kernel phase, applied on an integral field spectrograph, will be capable of simultaneous detection and characterization, and can reach separations much smaller than traditional IFS high contrast imaging. These techniques, applied on the next generation of adaptive optics systems and space- and ground-based observing facilities, will expand the planet detection parameter space in volume, semi-major axis, and contrast. Especially given the access to more distant, young stars, this will greatly inform our understanding of planet formation and evolution.

ACKNOWLEDGMENTS

Steph Sallum is supported by an NSF Astronomy and Astrophysics Postdoctoral Fellowship under award AST-1701489. The authors would like to acknowledge Zack Briesemeister and Jordan Stone for thoughtful conversations.

REFERENCES

[1] Skemer, A. J., Marley, M. S., Hinz, P. M., Morzinski, K. M., Skrutskie, M. F., Leisenring, J. M., Close, L. M., Saumon, D., Bailey, V. P., Briguglio, R., Defrere, D., Esposito, S., Follette, K. B., Hill, J. M., Males, J. R., Puglisi, A., Rodigas, T. J., and Xompero, M., "Directly Imaged L-T Transition Exoplanets in the Mid-infrared," ApJ **792**, 17 (Sept. 2014).

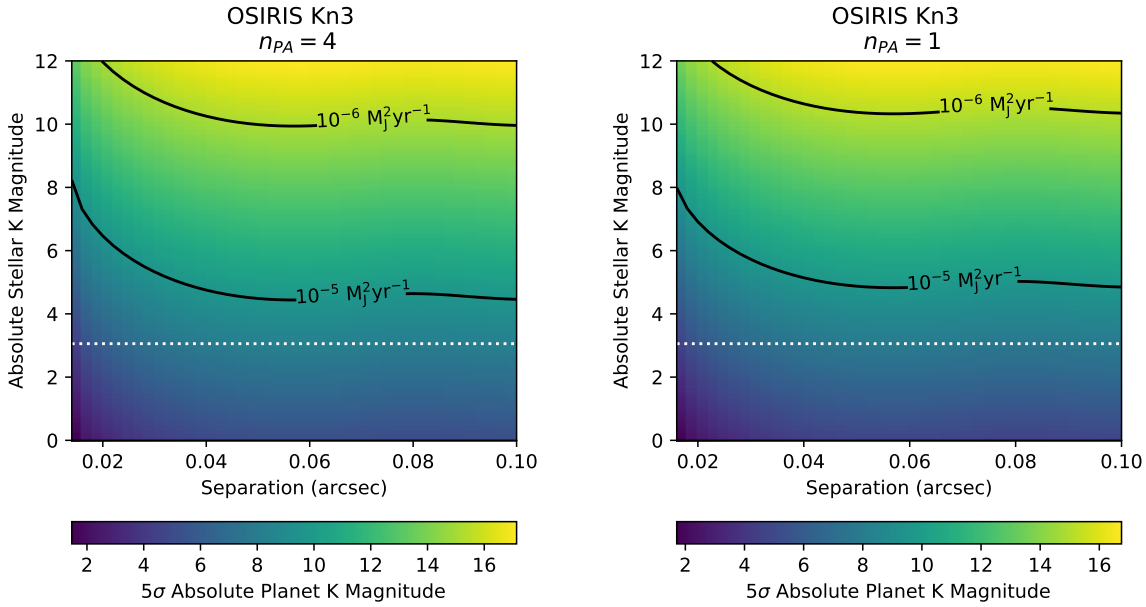

Figure 16 Circumplanetary accretion disk limits for 5σ contrast in the central Kn3 wavelength bin as a function of stellar absolute magnitude. The colorscale shows the 5σ planet absolute magnitude, and the contours show circumplanetary disk models. The left panel shows the four parallactic angle case, and the right shows the single snapshot case. The white dotted line shows the absolute magnitude of a 5 Myr old K5 star at a typical distance to nearby star forming regions ($\sim$ 140 pc).

[2] Fortney, J. J., Marley, M. S., Saumon, D., and Lodders, K., "Synthetic Spectra and Colors of Young Giant Planet Atmospheres: Effects of Initial Conditions and Atmospheric Metallicity," ApJ **683**, 1104–1116 (Aug. 2008).

[3] Zhu, Z., "Accreting Circumplanetary Disks: Observational Signatures," ApJ **799**, 16–24 (Jan. 2015).

[4] Eisner, J. A., "Spectral Energy Distributions of Accreting Protoplanets," ApJ **803**, L4–L8 (Apr. 2015).

[5] Marois, C., Lafrenière, D., Doyon, R., Macintosh, B., and Nadeau, D., "Angular Differential Imaging: A Powerful High-Contrast Imaging Technique," ApJ **641**, 556–564 (Apr. 2006).

[6] Guyon, O., Hinz, P. M., Cady, E., Belikov, R., and Martinache, F., "High Performance Lyot and PIAA Coronagraphy for Arbitrarily Shaped Telescope Apertures," ApJ **780**, 171 (Jan. 2014).

[7] Bowler, B. P., "Imaging Extrasolar Giant Planets," PASP **128**, 102001 (Oct. 2016).

[8] Torres, R. M., Loinard, L., Mioduszewski, A. J., and Rodríguez, L. F., "VLBA Determination of the Distance to Nearby Star-forming Regions. II. Hubble 4 and HDE 283572 in Taurus," ApJ **671**, 1813–1819 (Dec. 2007).

[9] Tuthill, P. G., Monnier, J. D., Danchi, W. C., Wishnow, E. H., and Haniff, C. A., "Michelson Interferometry with the Keck I Telescope," PASP **112**, 555–565 (Apr. 2000).

[10] Baldwin, J. E., Haniff, C. A., Mackay, C. D., and Warner, P. J., "Closure phase in high-resolution optical imaging," Nature **320**, 595–597 (Apr. 1986).

[11] Martinache, F., "Kernel Phase in Fizeau Interferometry," ApJ **724**, 464–469 (Nov. 2010).

[12] Ireland, M. J., "Phase errors in diffraction-limited imaging: contrast limits for sparse aperture masking," MNRAS **433**, 1718–1728 (Aug. 2013).

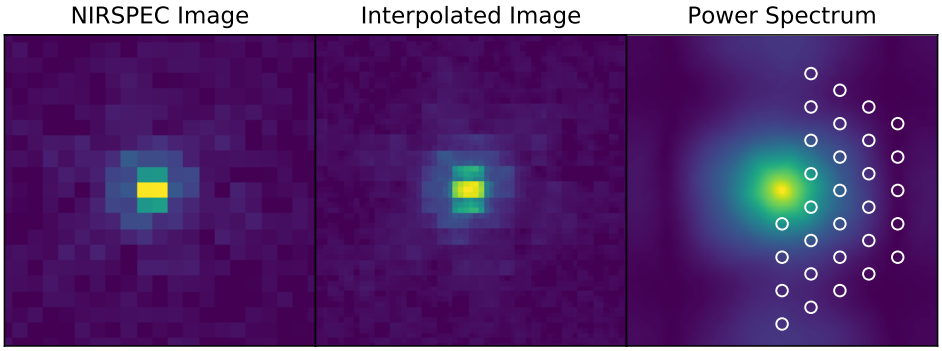

Figure 17 Individual NIRSpec image for a single integration (right), the interpolated image for a 5-point small grid dither using Modified Shepard weighting (center), and the resulting power spectrum (left). The imperfect interpolation leads to a decrease in power on the longest JWST baselines.

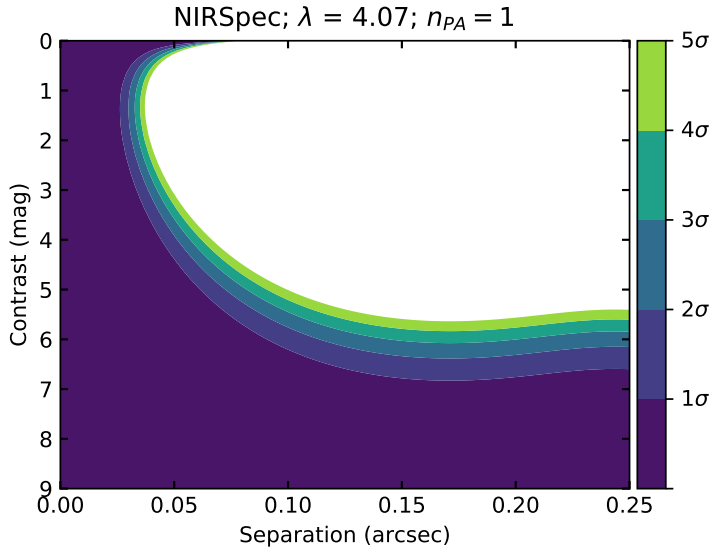

Figure 18 Contrast curves for a snapshot NIRSpec observation in the central wavelength bin ($\lambda_c = 4.07$ μm).

[13] Sallum, S., Eisner, J. A., Close, L. M., Hinz, P. M., Skemer, A. J., Bailey, V., Briguglio, R., Follette, K. B., Males, J. R., Morzinski, K. M., Puglisi, A., Rodigas, T. J., Weinberger, A. J., and Xompero, M., "New Spatially Resolved Observations of the T Cha Transition Disk and Constraints on the Previously Claimed Substellar Companion," ApJ **801**, 85–107 (Mar. 2015).

[14] Biller, B., Lacour, S., Juhász, A., Benisty, M., Chauvin, G., Olofsson, J., Pott, J.-U., Müller, A., Sicilia-Aguilar, A., Bonnefoy, M., Tuthill, P., Thebault, P., Henning, T., and Crida, A., "A Likely Close-in Low-mass Stellar Companion to the Transitional Disk Star HD 142527," ApJ **753**, L38 (July 2012).

[15] Kraus, A. L. and Ireland, M. J., "LkCa 15: A Young Exoplanet Caught at Formation?," ApJ **745**, 5–16 (Jan. 2012).

[16] Sallum, S., Follette, K. B., Eisner, J. A., Close, L. M., Hinz, P., Kratter, K., Males, J., Skemer, A., Macintosh, B., Tuthill, P., Bailey, V., Defrère, D., Morzinski, K., Rodigas, T., Spalding, E., Vaz, A., and

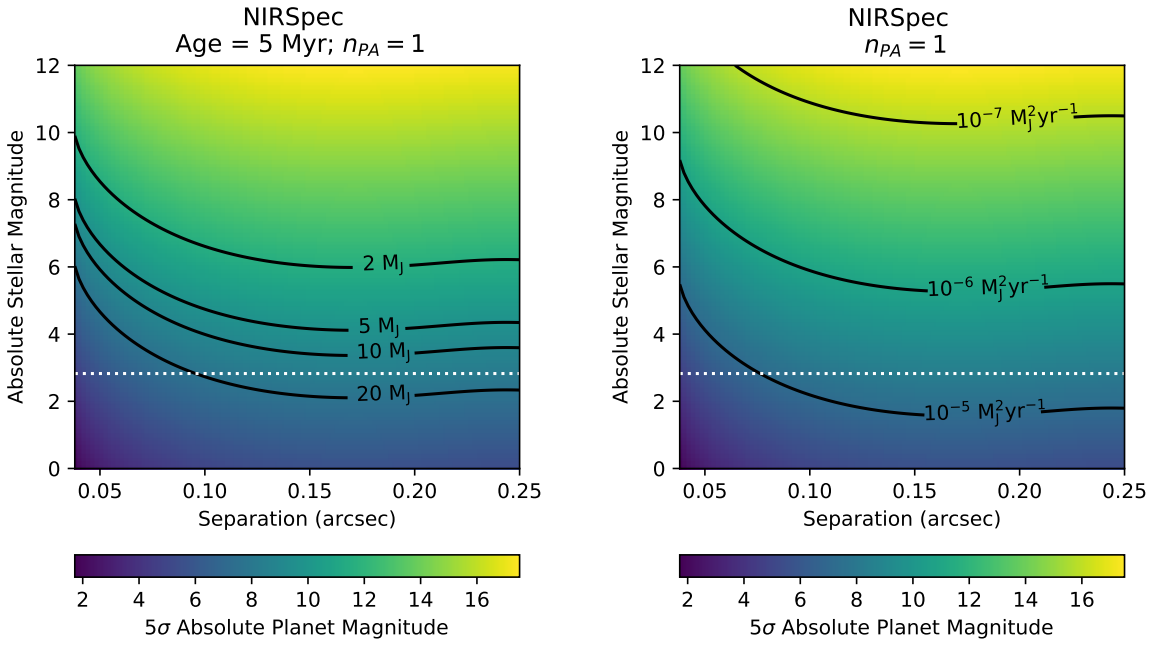

Figure 19 **Left:** Planet mass limits for 5σ contrast in the central NIRSpec wavelength bin as a function of stellar absolute magnitude. The colorscale shows the 5σ planet absolute magnitude, and the contours show DUSTY models for an age of 5 Myr. **Right:** Circumplanetary accretion disk limits for 5σ contrast in the central NIRSpec wavelength bin as a function of stellar absolute magnitude. The colorscale shows the 5σ planet absolute magnitude, and the contours show circumplanetary disk models. The white dotted line shows the absolute magnitude of a 5 Myr old K5 star at a typical distance to nearby star forming regions ($\sim$ 140 pc).

Weinberger, A. J., "Accreting protoplanets in the LkCa 15 transition disk," Nature **527**, 342–344 (Nov. 2015).

[17] Danchi, W. C., Tuthill, P. G., and Monnier, J. D., "Near-Infrared Interferometric Images of the Hot Inner Disk surrounding the Massive Young Star MWC 349A," ApJ **562**, 440–445 (Nov. 2001).

[18] Sallum, S., Eisner, J. A., Hinz, P. M., Sheehan, P. D., Skemer, A. J., Tuthill, P. G., and Young, J. S., "Improved Constraints on the Disk around MWC 349A from the 23 m LBTI," ApJ **844**, 22 (July 2017).

[19] Pope, B., Martinache, F., and Tuthill, P., "Dancing in the Dark: New Brown Dwarf Binaries from Kernel Phase Interferometry," ApJ **767**, 110 (Apr. 2013).

[20] Ireland, M. J. and Kraus, A. L., "Orbital Motion and Multi-Wavelength Monitoring of LkCa15 b," in [*IAU Symposium*], Booth, M., Matthews, B. C., and Graham, J. R., eds., *IAU Symposium* **299**, 199–203 (Jan. 2014).

[21] Pope, B., Tuthill, P., Hinkley, S., Ireland, M. J., Greenbaum, A., Latyshev, A., Monnier, J. D., and Martinache, F., "The Palomar kernel-phase experiment: testing kernel phase interferometry for ground-based astronomical observations," MNRAS **455**, 1647–1653 (Jan. 2016).

[22] Lamb, M. P., Correia, C., Sauvage, J.-F., Véran, J.-P., Andersen, D. R., Vigan, A., Wizinowich, P. L., van Dam, M. A., Mugnier, L., and Bond, C., "Quantifying telescope phase discontinuities external to adaptive optics systems by use of phase diversity and focal plane sharpening," *Journal of Astronomical Telescopes, Instruments, and Systems* **3**, 039001 (July 2017).

[23] Correia, C. M., Bond, C. Z., Sauvage, J.-F., Fusco, T., Conan, R., and Wizinowich, P. L., "Modeling astronomical adaptive optics performance with temporally filtered Wiener reconstruction of slope data," *Journal of the Optical Society of America A* **34**, 1877 (Oct. 2017).

[24] van Dam, M. A., Le Mignant, D., and Macintosh, B. A., "Performance of the Keck Observatory Adaptive-Optics System," Appl. Opt. **43**, 5458–5467 (Oct. 2004).

[25] Rampy, R., Ragland, S., Wizinowich, P., and Campbell, R., "Understanding and correcting low order residual static aberrations in adaptive optics corrected images," in [*Proceedings of the SPIE, Volume 9148, id. 91485I 17 pp. (2014).*], **9148**, 91485I (Aug. 2014).

[26] Baraffe, I., Chabrier, G., Barman, T. S., Allard, F., and Hauschildt, P. H., "Evolutionary models for cool brown dwarfs and extrasolar giant planets. The case of HD 209458," A&A **402**, 701–712 (May 2003).

[27] Herbig, G. H., Vrba, F. J., and Rydgren, A. E., "A spectroscopic survey of the Taurus-Auriga dark clouds for pre-main-sequence stars having CA II H, K emission," AJ **91**, 575–582 (Mar. 1986).

[28] Pontoppidan, K. M., Pickering, T. E., Laidler, V. G., Gilbert, K., Sontag, C. D., Slocum, C., Sienkiewicz, M. J., Hanley, C., Earl, N. M., Pueyo, L., Ravindranath, S., Karakla, D. M., Robberto, M., Noriega-Crespo, A., and Barker, E. A., "Pandeia: a multi-mission exposure time calculator for JWST and WFIRST," in [*Observatory Operations: Strategies, Processes, and Systems VI*], Proc. SPIE **9910**, 991016 (July 2016).

[29] Perrin, M. D., Soummer, R., Elliott, E. M., Lallo, M. D., and Sivaramakrishnan, A., "Simulating point spread functions for the James Webb Space Telescope with WebbPSF," in [*Space Telescopes and Instrumentation 2012: Optical, Infrared, and Millimeter Wave*], **8442**, 84423D (Sept. 2012).

[30] Greenbaum, A. Z., Pueyo, L., Sivaramakrishnan, A., and Lacour, S., "An Image-plane Algorithm for JWST's Non-redundant Aperture Mask Data," ApJ **798**, 68 (Jan. 2015).

[31] Marois, C., Nadeau, D., Doyon, R., Racine, R., and Walker, G. A. H., "Differential Simultaneous Imaging and Faint Companions: TRIDENT First Results from CFHT," in [*Brown Dwarfs*], Martín, E., ed., *IAU Symposium* **211**, 275–278 (June 2003).

[32] Biller, B. A., Close, L. M., Masciadri, E., Lenzen, R., Brandner, W., McCarthy, D., Henning, T., Nielsen, E. L., Hartung, M., Kellner, S., Geissler, K., and Kasper, M., "Contrast limits with the Simultaneous Differential Extrasolar Planet Imager (SDI) at the VLT and MMT," in [*Society of Photo-Optical Instrumentation Engineers (SPIE) Conference Series*], **6272**, 62722D (June 2006).

[33] Skemer, A. J., Hinz, P., Montoya, M., Skrutskie, M. F., Leisenring, J., Durney, O., Woodward, C. E., Wilson, J., Nelson, M., Bailey, V., Defrere, D., and Stone, J., "First light with ALES: A 2-5 micron adaptive optics Integral Field Spectrograph for the LBT," in [*Techniques and Instrumentation for Detection of Exoplanets VII*], **9605**, 96051D (Sept. 2015).

APPENDIX A. KERNEL PHASE HISTOGRAMS

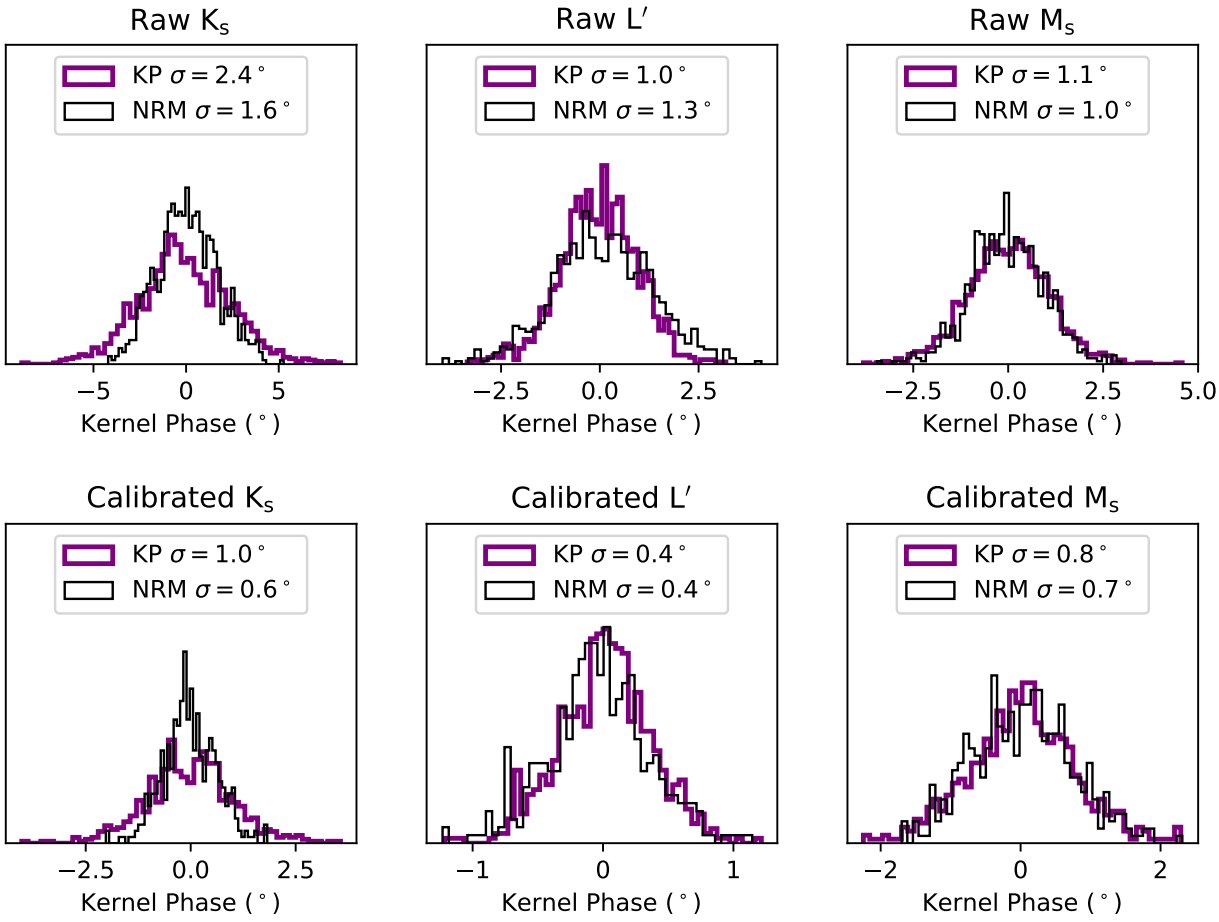

Figure A.1 Histograms of raw (top) and calibrated (bottom) kernel phases for K_s (left), L′ (middle), and M_s band (center) NIRC2 observations. Thick purple lines show filled-aperture kernel phases, while thin black lines show NRM kernel phases.

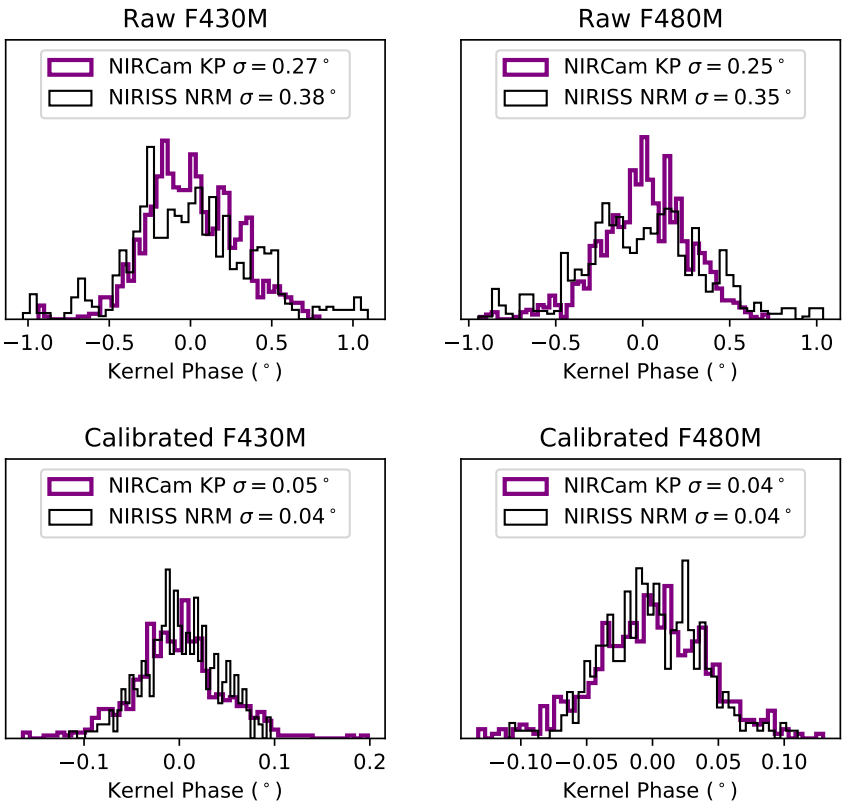

Figure A.2 Histograms of raw (top) and calibrated (bottom) kernel phases for F430M (left) and F480M band (right) observations. Thick purple lines show NIRCam filled-aperture kernel phases, while thin black lines show NIRISS NRM kernel phases.

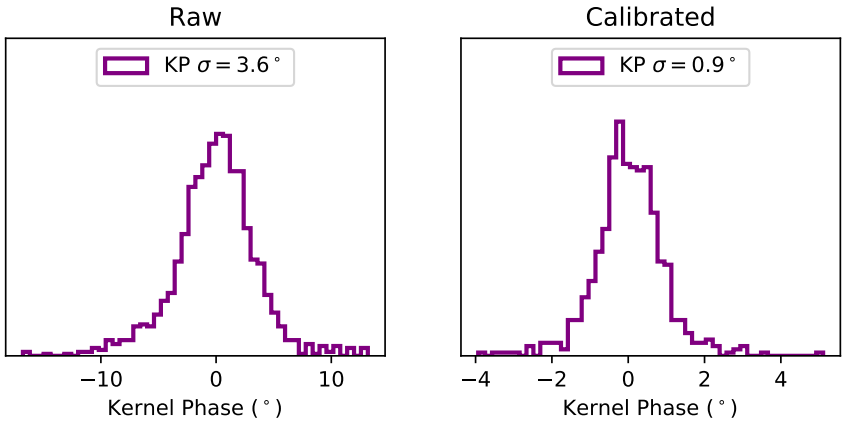

Figure A.3 Histograms of raw (left) and calibrated (right) kernel phases for simulated OSIRIS observations.

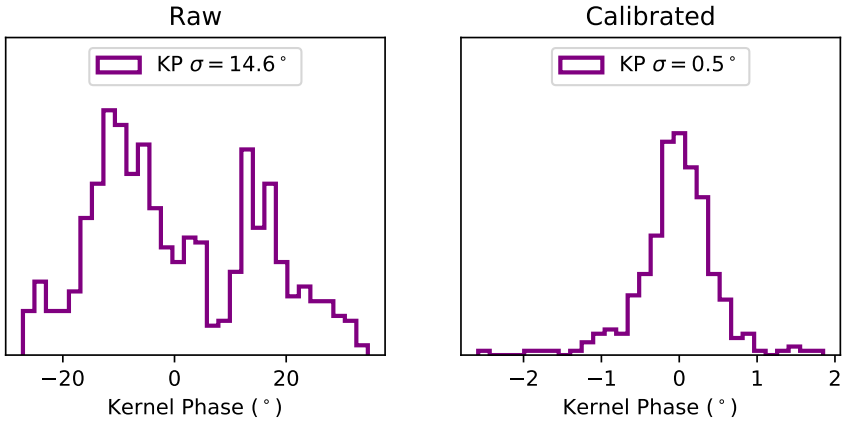

Figure A.4 Histograms of raw (left) and calibrated (right) kernel phases for simulated NIRSpec observations.